





Identifying regions of minimal backscattering by a relativistically moving sphere

Mitchell R. Whittam ^{1,*}, Aristeidis G. Lamprianidis,¹ Yannick Augenstein ¹ and Carsten Rockstuhl ^{1,2}

¹*Institut für Theoretische Festkörperphysik, Karlsruhe Institute of Technology, 76131 Karlsruhe, Germany*

²*Institute of Nanotechnology, Karlsruhe Institute of Technology, 76021 Karlsruhe, Germany*

 (Received 12 April 2023; revised 19 September 2023; accepted 25 September 2023; published 19 October 2023)

The far-field backscattering amplitude of an electric field from a relativistically moving sphere is analyzed. Contrary to prior research, we do so by expressing the fields in the helicity basis and we highlight here its advantages when compared to the commonly considered parity basis. With the purpose of exploring specific scattering phenomena considering relativistic effects, we identify conditions that minimize the backscattered field, leading to a relativistic formulation of the first Kerker condition. The requirements to be satisfied by the sphere are expressed in terms of Mie angles, which constitute an effective parametrization of any possible optical response a sphere might have. By considering different speeds of the sphere and angles of incidence, we are able to identify multiple combinations of Mie angles up to octupolar order via gradient-based optimization that satisfy our relativistic Kerker condition, that is, where the backscattered energy is at most 0.1% of the average scattered energy. Our results can be extended to involve multiple particles forming a metasurface, potentially having direct implications on the design of light sails as considered by the Breakthrough Starshot Initiative.

DOI: [10.1103/PhysRevA.108.043510](https://doi.org/10.1103/PhysRevA.108.043510)

I. INTRODUCTION

The scattering of light by a sphere is a canonical problem in optics and electrodynamics and has been investigated for many years, particularly for stationary spheres [1–11]. The scattering of light by spheres is best described using Mie theory, which involves expressing the incident and scattered electromagnetic fields in terms of vector spherical harmonics (VSHs). The amplitude coefficients that weight these VSHs are collected in a vector and are mutually linked by a matrix-vector product. Moreover, all optical properties of the object are captured by the corresponding matrix, called the transition or T matrix. For an arbitrary object, the T matrix can be dense, but it is diagonal for a sphere, and the diagonal entries are the Mie coefficients [12,13].

Controlling an object's geometrical and material properties provides a unique way of tailoring the scattered field on demand, and many intriguing aspects have been explored, an example being the so-called Kerker condition [14–18]. The first Kerker condition contains the necessary composition of multipolar excitations such that the object exhibits zero backscattering. A second Kerker condition implies a vanishing scattering in the forward direction, but this is considered less often, since optical gain is necessary for its observation [19].

While initially formulated for objects that can be safely described in dipolar approximation, it was soon realized that similar effects are encountered while capitalizing on higher-order multipole moments. This coined the notion of generalized Kerker conditions [20], and Kerker effects have been explored in a large variety of settings. These studies

are motivated by high-impact applications related to nanoantennas, chiral molecules, and metamaterials, to name a few [20–25].

This paper provides a further perspective on the Kerker effect. It considers the Kerker effect in the relativistic regime. The basic setting of our exploration is that of a relativistically moving sphere illuminated with a monochromatic Gaussian beam characterized by an angle of incidence Θ_i relative to the direction of motion of the sphere. Of course, unlike the case of a stationary sphere, one cannot assume that there exists a combination of multipole excitations that yield zero backscattering with the inclusion of motion. However, one can aim to minimize the backscattering, which depends on the multipolar contribution to the scattering response, for a given speed and field angle of incidence. This leads to an approximate Kerker condition in the case of a relativistically moving sphere.

Our work has clear implications for future technological developments. For example, within the Breakthrough Starshot Initiative [26,27], microgram satellites equipped with light sails, potentially made from metasurfaces consisting of a tailored arrangement of scatterers, are to be accelerated with an earth-based laser system up to a significant fraction of the speed of light. Using these satellites, neighboring galaxies would be explored. The design of such systems has many facets, and among them is the accurate description of the optical response from scattering objects in the form of metasurfaces. The formulation of the light scattering by an isolated object under relativistic conditions, as a pursuit in this contribution, is an important prerequisite to study such more advanced devices.

The structure of the paper is as follows. In Sec. II the physical setup is outlined and all necessary coordinate systems are defined. Moreover, the field of the considered incident beam is transformed from the laboratory frame to the reference

*mitchell.whittam@kit.edu

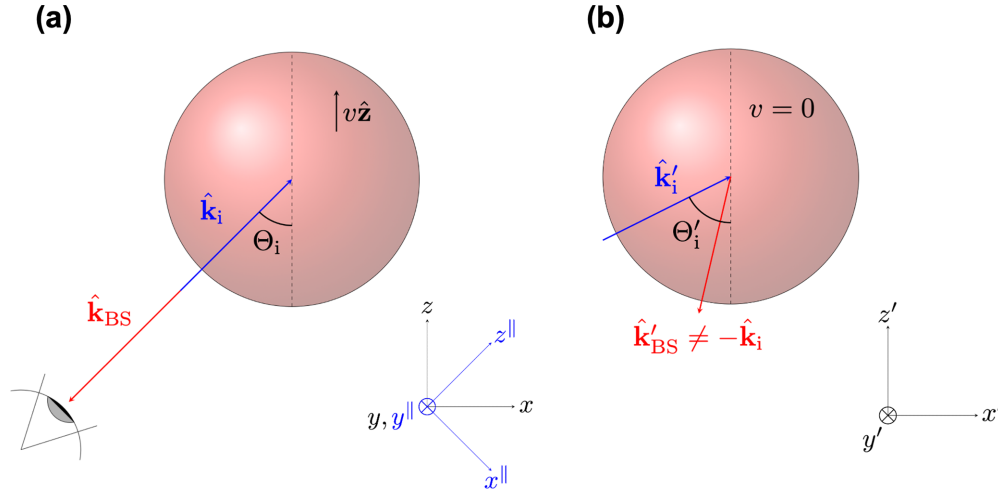


FIG. 1. Pictorial representation of the sphere in (a) the beam's frame S^{\parallel} and the rotated frame S containing an external observer (represented by the eye) and (b) the sphere's inertial reference frame S' . In S the sphere is seen to be moving with velocity $v\hat{z}$. The wave vector $\hat{\mathbf{k}}_i$ is incident on the sphere with angle Θ_i . In (a) the direction of backscattering $\hat{\mathbf{k}}_{BS}$ (denoted by the red arrow) is in the opposite direction to $\hat{\mathbf{k}}_i$ and it is this direction that is considered when formulating a relativistic Kerker condition. In (b) the sphere is stationary ($v = 0$) in S' , while the Lorentz-boosted wave vector of the incident field is given by $\hat{\mathbf{k}}'_i$ and is incident with angle $\Theta'_i \neq \Theta_i$ when $\Theta_i \notin \{0, \pi\}$ and $\Theta'_i = \Theta_i$ when $\Theta_i \in \{0, \pi\}$. Moreover, the direction of backscattering $\hat{\mathbf{k}}'_{BS}$ in this frame is in general not opposite to $\hat{\mathbf{k}}_i$ or $\hat{\mathbf{k}}'_i$. (a) Frames S^{\parallel} and S and (b) Frame S' .

frame of the sphere based on the transformation of each constitutive plane wave of its angular spectrum representation. Afterward, the scattered field is obtained by solving an ordinary Mie problem in the rest frame of the sphere. We rely on a parametrization of its response using Mie angles [28]. These Mie angles constitute a minimalist model to express all possible responses from a sphere, which allows a generic analysis of the backscattering response. To conclude Sec. II, the scattered field will be transformed back to the laboratory frame, in which the backscattering is observed.

In Sec. III the backscattering amplitude is visualized with respect to some given Mie angles for a sphere with a fixed velocity and a field with a fixed angle of incidence. An explicit example of the backscattering as a function of the radius of a spherical particle made of silicon carbide is also considered. We implement all calculations using the JULIA programming language [29] and implement a gradient-based optimization scheme by leveraging automatic differentiation within the JUMP modeling framework [30], much in the spirit of recent works on differentiable physics solvers [31,32]. Using this scheme, we design spheres that provide minimum values for the backscattering and identify the corresponding combinations of Mie angles. We find multiple suitable combinations by considering different speeds of the sphere and angles of incidence, where the suitability is defined by a backscattering which contributes at most 0.1% to the average scattered energy. In Sec. IV we summarize our findings.

II. DESCRIPTION OF THE SCATTERING SCENARIO

Before delving into the mathematical description of the scattered field, it is first necessary to specify the geometry and constraints of the system. We consider a spherical particle moving at a relativistic velocity $\mathbf{v} = v\hat{z}$ within a pervading incident electric field $\mathbf{E}_i(\mathbf{r}, t)$ with angle of incidence Θ_i

as observed by an external laboratory frame S . Although an accompanying magnetic field will always exist, to avoid repetition, we omit explicit reference to this. Two additional frames are considered, namely, the beam's frame S^{\parallel} , which is the frame where the direction of motion of the beam moves parallel to its corresponding z^{\parallel} axis, and the boosted frame S' , which represents the inertial reference frame of the sphere (see Fig. 1). Accordingly, the corresponding quantities are denoted without a prime in S and with a prime in S' , while all quantities in S^{\parallel} are denoted with a \parallel superscript.

Another quantity of interest is the polar angle Θ_i between $\hat{\mathbf{k}}_i$ and \mathbf{v} , i.e., the angle between the beam's propagation direction and the axis of movement of the scatterer (see Fig. 1). Given the symmetry of the system, we set the azimuthal angle of the incident field Φ_i to be zero. Moreover, the direction of backscattering is given by $\hat{\mathbf{k}}_{BS}$, the opposite direction to $\hat{\mathbf{k}}_i$.

To determine the scattered field in S , we implement the frame-hopping method (FHM) as described by Garner *et al.* [33]. For reference, this process is outlined below.

- (1) Lorentz boost the incident electric field from S to S' .
- (2) Solve the scattering problem in S' .
- (3) Inverse Lorentz boost the scattered field from S' back to S .

The reason for computing the scattered field in S' and not S is a matter of mathematical simplicity. In S' , the scattering calculation is analogous to a stationary system, thus avoiding any superfluous variable transformations.

A. Lorentz boosting the incident field into the scatterer's reference frame

First, we need to consider the incident field in the beam's reference frame S^{\parallel} . As an incident field, we consider a single monochromatic Gaussian beam of well-defined helicity (i.e., handedness) expanded in terms of circularly polarized plane

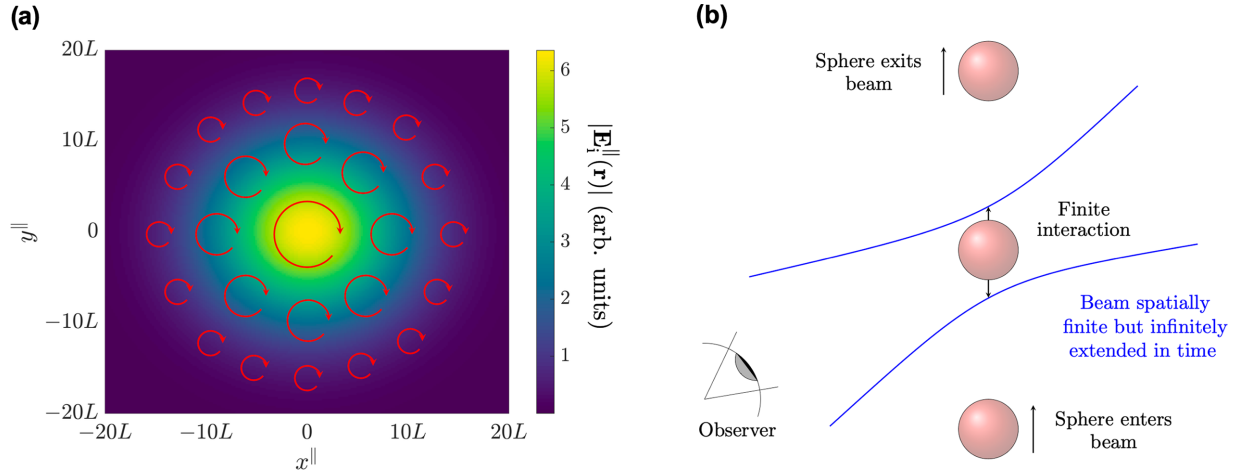


FIG. 2. (a) Amplitude in the form of a transverse cross section of the incident beam given by $|\mathbf{E}_i^{\parallel}(\mathbf{r})|$ with arbitrary wavelength L and waist $w_0 = 10L$. The overlaying red arrows depict the left-handed circular polarization of the beam ($\lambda_i = +1$) scaled with $|\mathbf{E}_i^{\parallel}(\mathbf{r})|$. (b) Schematic for the finite interaction between the sphere and the incident beam.

waves, which are eigenstates of the electromagnetic wave equation. We use the ket in abstract Dirac notation to denote such plane waves as eigenstates of free space characterized by helicity $\lambda^{\parallel} = \pm 1$, temporal frequency ω^{\parallel} , and direction of propagation $\hat{\mathbf{k}}^{\parallel}$,

$$|\lambda^{\parallel} \hat{\mathbf{k}}^{\parallel} \omega^{\parallel}\rangle \doteq \hat{\mathbf{e}}_{\lambda^{\parallel}}(\hat{\mathbf{k}}^{\parallel}) \exp\{i\omega^{\parallel}[(\hat{\mathbf{k}}^{\parallel} \cdot \mathbf{r}/c) - t]\}, \quad (1)$$

where the symbol \doteq refers to the spatiotemporal representation of the plane-wave eigenstate. The quantity c is the speed of light in a vacuum, and the polarization unit vector $\hat{\mathbf{e}}_{\lambda^{\parallel}}(\hat{\mathbf{k}}^{\parallel})$ is given by

$$\hat{\mathbf{e}}_{\lambda^{\parallel}}(\hat{\mathbf{k}}^{\parallel}) = \frac{-\lambda^{\parallel} \hat{\theta}(\hat{\mathbf{k}}^{\parallel}) - i\hat{\phi}(\hat{\mathbf{k}}^{\parallel})}{\sqrt{2}}, \quad (2)$$

where $\lambda^{\parallel} = \pm 1$ corresponds to left or right circularly polarized waves. The quantities $\hat{\theta}$ and $\hat{\phi}$ are the polar and azimuthal spherical unit vectors perpendicular to the direction of propagation $\hat{\mathbf{k}}^{\parallel}$ that is characterized by the polar and azimuthal angles of propagation θ^{\parallel} and ϕ^{\parallel} of each constituent plane wave, respectively. Such fields of well-defined helicity are known as Beltrami fields and obey Eq. (A6) [34–37]. Throughout all the following calculations, we consider an incident field of pure helicity $\lambda_i = +1$.

Likewise denoting all remaining quantities that belong to the incident field by the subscript i , we represent a general electric field in terms of its angular spectrum, i.e., as a plane-wave expansion

$$|\mathbf{E}_i^{\parallel}\rangle = \sum_{\lambda} \int_0^{2\pi} d\phi^{\parallel} \int_0^{\pi} d\theta^{\parallel} \int_{0^+}^{\infty} d\omega^{\parallel} \mathcal{G}_{\lambda^{\parallel}, i}^{\parallel}(\omega^{\parallel}, \theta^{\parallel}, \phi^{\parallel}) |\lambda^{\parallel} \hat{\mathbf{k}}^{\parallel} \omega^{\parallel}\rangle + \text{c.c.}, \quad (3)$$

where the amplitudes for a monochromatic Gaussian beam focused at the origin of S of waist w_0 , frequency ω_i , and

helicity λ_i propagating along the $+z$ axis are given by

$$\begin{aligned} \mathcal{G}_{\lambda^{\parallel}, i}^{\parallel}(\omega^{\parallel}, \theta^{\parallel}, \phi^{\parallel}) &= E_0 \sin(2\theta^{\parallel}) \\ &\times \exp\left(i\lambda_i \phi^{\parallel} - \frac{\omega_i^2 w_0^2 \sin^2(\theta^{\parallel})}{4c^2}\right) \\ &\times \delta_{\lambda^{\parallel} \lambda_i} \delta(\omega^{\parallel} - \omega_i) H(\pi/2 - \theta^{\parallel}), \end{aligned} \quad (4)$$

where E_0 is a constant and $H(\pi/2 - \theta^{\parallel})$ is the Heaviside step function which eliminates all counterpropagating waves. The phase term $\exp(i\lambda_i \phi^{\parallel})$ is introduced to assign the beam an angular momentum of $m_z = \lambda_i$, as is the case of a circularly polarized plane wave in the limit of a very large beam waist w_0 , which is what we consider here. The large w_0 means that $|\mathbf{E}_i^{\parallel}\rangle$ approximates to a plane wave but is nonetheless still finite in space. Specifically, we consider a waist given by $w_0 = 10L$, where L is the wavelength of the beam. In Fig. 2(a) the transverse magnitude profile of the beam $|\mathbf{E}_i^{\parallel}(\mathbf{r})|$ can be seen for arbitrary L at time $t = 0$, along with red arrows depicting the left-handed circular polarization due to the helicity $\lambda_i = +1$. One sees here very clearly the finite spatial nature of the beam.

The reason for considering such an incident field instead of a regular plane wave infinitely extended in space is that the interaction of the incident wave with the moving sphere would, in the latter case, be incessant. Consequently, the scattered power flux would have a cylindrical symmetry with respect to the axis of movement of the scatterer, that is, the scattered power flux would be translationally invariant with respect to this axis and would only vary azimuthally. On the other hand, an excitation of finite spatial extent ensures that the interaction of light with the scatterer is localized in space (around the origin of S), therefore yielding a spherical-like scattering of waves emanating from the region where the interaction takes place. Moreover, the monochromaticity of the beam implies it is infinitely extended in time t . This temporal omnipresence coupled with the finite spatial nature of the beam means the sphere simply goes in through one part of the beam and out

of another, thus making the interaction finite. This process is visualized in Fig. 2(b).

To consider an electric field of arbitrary angle of incidence Θ_i , we apply a rotation operator $\hat{\mathbf{R}}_y(\Theta_i)$ about the y axis to Eq. (3) to transit from a representation of the beam with respect to S^\parallel to one with respect to S such that

$$|\mathbf{E}_i\rangle = \hat{\mathbf{R}}_y(\Theta_i)|\mathbf{E}_i^\parallel\rangle, \quad (5)$$

where

$$\hat{\mathbf{R}}_y(\Theta_i)|\lambda^\parallel\hat{\mathbf{k}}^\parallel\omega^\parallel\rangle = \sum_\lambda \int_0^{2\pi} d\phi \int_0^\pi d\theta \int_{0^+}^\infty d\omega \mathcal{R}_{\lambda^\parallel,\lambda}(\omega^\parallel, \theta^\parallel, \phi^\parallel, \omega, \theta, \phi; \Theta_i)|\lambda\hat{\mathbf{k}}\omega\rangle. \quad (6)$$

The transformation coefficients are given by

$$\begin{aligned} \mathcal{R}_{\lambda^\parallel,\lambda}(\omega^\parallel, \theta^\parallel, \phi^\parallel, \omega, \theta, \phi; \Theta_i) \\ = \mathcal{P}(\theta^\parallel, \phi^\parallel, \Theta_i)\delta_{\lambda^\parallel\lambda}\delta(\omega - \omega^\parallel) \\ \times \delta(\theta - \arccos(\hat{k}_z))\delta(\phi - \arctan2(\hat{k}_y, \hat{k}_x)), \end{aligned} \quad (7)$$

where

$$\begin{aligned} \begin{pmatrix} \hat{k}_x \\ \hat{k}_y \\ \hat{k}_z \end{pmatrix} &= \begin{pmatrix} \cos\Theta_i & 0 & \sin\Theta_i \\ 0 & 1 & 0 \\ -\sin\Theta_i & 0 & \cos\Theta_i \end{pmatrix} \begin{pmatrix} \hat{k}_x^\parallel \\ \hat{k}_y^\parallel \\ \hat{k}_z^\parallel \end{pmatrix} \\ &= \begin{pmatrix} \sin\theta^\parallel \cos\phi^\parallel \cos\Theta_i + \cos\theta^\parallel \sin\Theta_i \\ \sin\theta^\parallel \sin\phi^\parallel \\ -\sin\theta^\parallel \cos\phi^\parallel \sin\Theta_i + \cos\theta^\parallel \cos\Theta_i \end{pmatrix} \end{aligned} \quad (8)$$

and $\mathcal{P}(\theta^\parallel, \phi^\parallel, \Theta_i)$ is a prefactor corresponding to the acquired phase due to the rotation

$$\mathcal{P}(\theta^\parallel, \phi^\parallel, \Theta_i) = \exp[ip(\theta^\parallel, \phi^\parallel, \Theta_i)], \quad (9)$$

with

$$\begin{aligned} p(\theta^\parallel, \phi^\parallel, \Theta_i) &= \arctan2[-\lambda \sin(\Theta_i) \sin(\phi^\parallel), \cos(\theta^\parallel)] \\ &\times \sin(\Theta_i) \cos(\phi^\parallel) + \sin(\theta^\parallel) \cos(\Theta_i). \end{aligned} \quad (10)$$

After doing this, one can follow the first step of the frame-hopping method and compute the Lorentz boost of the incident electric field from S to S' . In Appendix A we calculate the Lorentz boost of plane waves. We denote by $\hat{\mathbf{B}}_z(\beta)$ the operator that boosts fields along the z axis with speed $v = \beta c$ from S to S' , where $0 \leq \beta < 1$. This operator acts on the eigenstates of monochromatic plane waves with well-defined helicity in the following way:

$$\begin{aligned} \hat{\mathbf{B}}_z(\beta)|\lambda\hat{\mathbf{k}}\omega\rangle &= \sum_{\lambda'} \int_0^{2\pi} d\phi' \int_0^\pi d\theta' \int_{0^+}^\infty d\omega' \mathcal{L}_{\lambda\lambda'} \\ &(\omega, \theta, \phi, \omega', \theta', \phi'; \beta)|\lambda'\hat{\mathbf{k}}'\omega'\rangle. \end{aligned} \quad (11)$$

The transformation coefficients are given by

$$\begin{aligned} \mathcal{L}_{\lambda\lambda'}(\omega, \theta, \phi, \omega', \theta', \phi'; \beta) \\ = \mathcal{C}(\beta, \theta)\delta_{\lambda\lambda'}\delta(\omega' - \mathcal{C}(\beta, \theta)\omega) \\ \times \delta\left(\theta' - \arccos\left(\frac{\cos\theta - \beta}{1 - \beta\cos\theta}\right)\right)\delta(\phi' - \phi), \end{aligned} \quad (12)$$

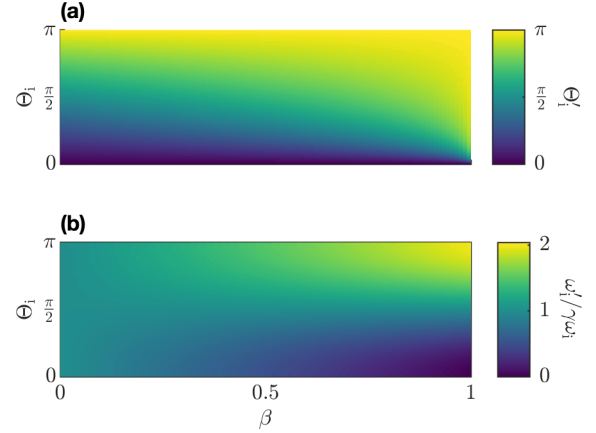


FIG. 3. (a) Doppler shift Θ'_i of Θ_i as a function of Θ_i and β determined using Eq. (14). This demonstrates that the direction of the incident wave as perceived in S' is different from that in S . (b) Normalized Doppler-shifted incident frequency $\omega'_i/\gamma\omega_i$ as a function of Θ_i and β , where ω'_i is the Doppler-shifted incident frequency determined using Eq. (15). When $\Theta_i = 0$ and $\beta \rightarrow 1$, the object is moving away from the field source, thus causing the incident frequency in S' to decrease (redshift). When $\Theta_i = \pi$ and $\beta \rightarrow 1$, the object is moving towards the field source, thus causing the incident frequency in S' to increase (blueshift). When $\Theta_i = \pi/2$, $\omega'_i/\gamma\omega_i = 1$ for all β . This is due to $\hat{\mathbf{k}}_i$ and \mathbf{v} being perpendicular to each other. The factor $1/\gamma$ is necessary to eliminate the exaggeration of ω'_i when $\beta \rightarrow 1$ and $\Theta_i \rightarrow \pi$. Without this factor, the other frequency values would appear too suppressed.

where $\gamma = 1/\sqrt{1 - \beta^2}$, $\cos\theta = \hat{\mathbf{k}} \cdot \hat{\mathbf{z}}$, and

$$\mathcal{C}(\beta, \theta) = \gamma(1 - \beta\cos\theta), \quad (13)$$

which is derived in Appendix A. We see from Eq. (12) that

$$\theta' = \arccos\left(\frac{\cos\theta - \beta}{1 - \beta\cos\theta}\right) \quad (14)$$

and

$$\omega' = \mathcal{C}(\beta, \theta)\omega \quad (15)$$

correspond to the Lorentz boost of θ and ω , respectively. Since the motion occurs solely along the z axis, the azimuthal angle ϕ remains unchanged under the Lorentz boost, that is,

$$\phi' = \phi. \quad (16)$$

The Lorentz boost θ' of θ given by Eq. (14) explains the perceived change in direction of the beam in S' compared to S as shown by $\hat{\mathbf{k}}_i$ and $\hat{\mathbf{k}}'_i$ in Fig. 1. In Fig. 3(a) this is visualized for the Lorentz boost Θ'_i of the polar angle of the incident field with respect to the angle of incidence Θ_i as seen in S and speed ratio β . Moreover, the Doppler shift ω' of ω is displayed in Fig. 3(b) with the same functional dependence. Note that, for an angle of incidence of $\Theta_i = 0$ and a speed ratio $\beta \rightarrow 1$, the Doppler-shifted frequency becomes zero. This corresponds to the sphere moving away from the external observer in S at a speed tending to that of light, thus exhibiting a complete redshift. In other words, the incident wave is perceived by the sphere to be so stretched out that the frequency disappears in its reference frame. Conversely, when $\Theta_i = \pi$

and $\beta \rightarrow 1$, the wave is seen to be infinitely blueshifted in S' , corresponding to a completely compressed wave with infinite frequency. This corresponds to the sphere moving towards the source of the incident field.

Note that the same expression for the scaling factor $\mathcal{C}(\beta, \theta)$ is given by Eq. (27) in [38]. Importantly, we observe that for Eq. (12) to be nonzero, the helicity of the field must remain invariant upon the Lorentz boost transformation due to the $\delta_{\lambda'\lambda}$ term. This invariance demonstrates the power of expressing the fields in the helicity basis using Beltrami fields instead of the parity basis, that is, specifically making use of circularly polarized plane waves instead of TE/TM plane waves.

Generally speaking, the change in direction of the beam upon boosting is given by the following transformation of the wave vectors:

$$\hat{\mathbf{k}}' = \frac{\hat{\mathbf{k}} + [(\gamma - 1)\cos\theta - \gamma\beta]\hat{\mathbf{z}}}{\mathcal{C}(\beta, \theta)}. \quad (17)$$

Finally, putting all the above together, and after some straightforward algebra, we can get the relation between the amplitudes of the initially considered and nonrotated incident beam in S^\parallel and the rotated one in S' ,

$$\begin{aligned} |\mathbf{E}'_i\rangle &= \hat{\mathbf{B}}_z(\beta)\hat{\mathbf{R}}_y(\Theta_i)|\mathbf{E}_i\rangle \\ &= \sum_{\lambda'} \int_0^{2\pi} d\phi' \int_0^\pi d\theta' \int_{0^+}^\infty d\omega' \mathcal{G}'_{\lambda',i}(\omega', \theta', \phi') |\lambda'_i \hat{\mathbf{k}}'_i \omega'_i\rangle \\ &\quad + \text{c.c.}, \end{aligned} \quad (18)$$

where ω'_i and $\hat{\mathbf{k}}'_i$ are determined by Eqs. (15) and (17), respectively, and

$$\begin{aligned} \mathcal{G}'_{\lambda',i}(\omega', \theta', \phi') &= \mathcal{J}(\theta', \phi', \Theta_i) \mathcal{G}_{\lambda',i}^\parallel \left(\frac{\omega'}{\mathcal{C}[\beta, \theta^\parallel(\theta', \phi')]} , \theta^\parallel(\theta', \phi'), \right. \\ &\quad \left. \phi^\parallel(\theta', \phi') \right), \end{aligned} \quad (19)$$

where $\theta^\parallel(\theta', \phi')$ and $\phi^\parallel(\theta', \phi')$ express θ^\parallel and ϕ^\parallel as viewed from S' ,

$$\begin{aligned} \theta^\parallel(\theta', \phi') &= \arccos \left(\frac{1}{\gamma(1 + \beta \cos \theta')} [\sin \theta' \cos \phi' \sin \Theta \right. \\ &\quad \left. + \gamma(\cos \theta' + \beta) \cos \Theta] \right), \end{aligned} \quad (20)$$

$$\begin{aligned} \phi^\parallel(\theta', \phi') &= \arctan 2[\sin \theta' \sin \phi', \sin \theta' \cos \phi' \cos \Theta \\ &\quad - \gamma(\cos \theta' + \beta) \sin \Theta], \end{aligned} \quad (21)$$

with the Jacobian

$$\begin{aligned} \mathcal{J}(\theta', \phi', \Theta_i) &= \begin{vmatrix} \frac{\partial \theta^\parallel}{\partial \theta'} & \frac{\partial \theta^\parallel}{\partial \phi'} & \frac{\partial \theta^\parallel}{\partial \omega'} \\ \frac{\partial \phi^\parallel}{\partial \theta'} & \frac{\partial \phi^\parallel}{\partial \phi'} & \frac{\partial \phi^\parallel}{\partial \omega'} \\ \frac{\partial \omega^\parallel}{\partial \theta'} & \frac{\partial \omega^\parallel}{\partial \phi'} & \frac{\partial \omega^\parallel}{\partial \omega'} \end{vmatrix} \\ &= \frac{1}{\mathcal{C}[\beta, \theta(\theta')]} \begin{vmatrix} \frac{\partial \theta^\parallel}{\partial \theta'} & \frac{\partial \theta^\parallel}{\partial \phi'} \\ \frac{\partial \phi^\parallel}{\partial \theta'} & \frac{\partial \phi^\parallel}{\partial \phi'} \end{vmatrix} \end{aligned} \quad (22)$$

that converts $d\phi^\parallel d\theta^\parallel$ to $d\phi' d\theta'$, where $\omega^\parallel = \omega$.

Recall that we do this since, for simplicity, we wish to carry out the scattering calculation in S' , that is, where it is equivalent to that in the stationary case. For a given incident field described by Eq. (3), we can use Eq. (19) to calculate the amplitudes that are needed to describe the incident field in S' in terms of the plane-wave representation given by Eq. (18).

B. Solving the scattering problem in the sphere's reference frame

The approach taken to calculate the amplitude of the scattered field begins by expressing the incident field $|\mathbf{E}'_i\rangle$ as a series of spherical waves with respect to the coordinates describing S' [12],

$$|\mathbf{E}'_i\rangle = \sum_{\lambda'\ell'm'} \int_{0^+}^\infty d\omega' \mathcal{A}'_{\lambda'\ell'm'}(\omega') |\omega'\lambda'\ell'm'\rangle^{(1)} + \text{c.c.}, \quad (23)$$

where $|\omega'\lambda'\ell'm'\rangle^{(1)}$ signifies a regular VSH attached to S' with frequency ω' , helicity λ' , multipolar index ℓ' ($\ell' = 1$ corresponds to dipoles, $\ell' = 2$ corresponds to quadrupoles, etc.), and angular momentum along the z axis $m' = -\ell', -(\ell' - 1), \dots, \ell'$. The superscript (1) denotes that the VSH corresponds to a first-order spherical Bessel function $j_\ell(k'r')$, and the coefficients of the expansion are given by

$$\mathcal{A}'_{\lambda'\ell'm'}(\omega') = \int_0^{2\pi} d\phi' \int_0^\pi d\theta' \mathcal{G}'_{\lambda',i}(\omega', \theta', \phi') \mathcal{S}_{\lambda'\ell'm'}(\omega', \hat{\mathbf{k}}'), \quad (24)$$

where the transformation coefficients between the plane waves and the spherical waves (under which transformation the helicity and frequency of the waves remain unchanged) are given by

$$\mathcal{S}_{\lambda'\ell'm'}(\theta', \phi') = 4\pi i^{\ell'+2m'-1} \Omega_{\ell'm'} \tau_{\ell'm'}^{(\lambda')}(\theta') e^{-im'\phi'}, \quad (25)$$

where $\Omega_{\ell'm'}$ is a normalization constant and $\tau_{\ell'm'}^{(\lambda')}(\theta')$ is a function which we define in Appendix B. The expression given in Eq. (25) is derived by applying Eq. (2) to Eq. (12) in [39].

Note that we choose to use Beltrami fields in this case. While the standard Lorenz-Mie language, where TE and TM waves are implemented, is a perfectly valid notation, we opted for the former. The reason for this is, since the helicity is invariant under Lorentz boosts [40], one has one fewer transformation to consider when inverse boosting from S' to S in Sec. II C. Furthermore, the boosting operator given by Eq. (11) is diagonal with respect to helicity, which is not the case with TE and TM waves. Therefore, we believe the usage of Beltrami fields allows for a cleaner solution.

For the case of a monochromatic excitation (in S), like the one we consider here, we have from Eq. (4) that

$$\mathcal{G}'_{\lambda',i}(\omega^\parallel, \theta^\parallel, \phi^\parallel) = \mathcal{G}'_{\lambda',i}{}^{\parallel,0}(\theta^\parallel, \phi^\parallel) \delta(\omega^\parallel - \omega_i). \quad (26)$$

Using this expression, we get the simplified expression for the incident spherical amplitudes in S' ,

$$\begin{aligned} \mathcal{A}'_{\lambda'\ell'm'}(\omega') &= 4\pi i^{\ell'+2m'-1} \Omega_{\ell'm'} \tau_{\ell'm'}^{(\lambda')}(\theta'_0) \delta\left(\omega' \in \left[\frac{\omega_i}{\gamma(1+\beta)}, \frac{\omega_i}{\gamma(1-\beta)}\right]\right) \frac{1}{\beta\gamma\omega' \mathcal{C}(-\beta, \theta'_0) \sin\theta'_0} \mathcal{C}[\beta, \theta(\theta'_0)] \\ &\times \int_0^{2\pi} d\phi' e^{-im'\phi'} \mathcal{P}[\theta^\parallel(\theta'_0, \phi'), \phi^\parallel(\theta'_0, \phi'), \Theta_i] \mathcal{J}(\theta'_0, \phi', \Theta_i) \mathcal{G}_{\lambda',i}^{\parallel,0}[\theta^\parallel(\theta'_0, \phi'), \phi^\parallel(\theta'_0, \phi')], \end{aligned} \quad (27)$$

where

$$\theta'_0(\omega') = \arccos\left(\frac{\omega_i - \gamma\omega'}{\beta\gamma\omega'}\right). \quad (28)$$

Next, in conjunction with step 2 of the FHM, we need to express the scattered field $|\mathbf{E}'_s\rangle$ as a series of radiating VSHs in S' , denoted by $|\omega'\lambda'\ell'm'\rangle^{(3)}$. Analogous to Eq. (23), this can be written as

$$|\mathbf{E}'_s\rangle = \sum_{\lambda'\ell'm'} \int_{0^+}^{\infty} d\omega' \mathcal{B}'_{\lambda'\ell'm'}(\omega') |\omega'\lambda'\ell'm'\rangle^{(3)} + \text{c.c.}, \quad (29)$$

where the (3) superscript denotes that the VSHs correspond to a third-order spherical Bessel (Hankel) function $h_\ell(k'r')$. Specific expressions of the radiating and regular VSHs are given in Appendix B. Moreover, the subscript s denotes quantities which correspond to the scattered field.

Finally, the scattering coefficients $\mathcal{B}'_{\lambda'\ell'm'}(\omega')$ can be related to the incident coefficients $\mathcal{A}'_{\lambda'\ell'm'}(\omega')$ by way of the T -matrix formalism [12]

$$\mathbf{B}' = \mathbf{T}^H \mathbf{A}', \quad (30)$$

where \mathbf{A}' and \mathbf{B}' are vectors containing the incident and scattering coefficients, respectively, and \mathbf{T}^H is the corresponding T matrix expressed in the helicity basis (see [41,42] and Appendix C). The T matrix fully describes the scattering response of the individual scatterer in the stationary case, which we can safely use in the rest frame of the sphere. Let us note that the time invariance of the stationary system implies a matrix that is diagonal with respect to frequency ω' , whereas duality symmetry implies a diagonal matrix with respect to helicity λ' and the spherical symmetry of the scatterer implies a diagonal matrix with respect to the multipolar indices ℓ' and m' .

Specifically, for a spherical scatterer, we can write

$$\mathcal{B}'_{\lambda'\ell'm'}(\omega') = \sum_{\lambda_0} T_{\lambda'\lambda_0,\ell'}(\omega') \mathcal{A}_{\lambda_0\ell'm'}(\omega'), \quad (31)$$

where $\lambda_0 = \pm 1$ is a dummy index representing helicity and the term $T_{\lambda'\lambda_0,\ell'}$ is defined at the end of Appendix C. Moreover, in this work, we will make the assumption that the T matrix of the scatterer is nondispersive, i.e., invariant with respect to frequency. This assumption is logical as long as we are exciting with a monochromatic beam with a narrow angular spectrum, i.e., a large waist. One must consider this, since the plane-wave components of the beam all Doppler shift differently depending on their polar angles of propagation. However, a small angular width in S minimizes this difference, thus allowing us to assume a nondispersive T matrix in S' . As we will see, this assumption significantly simplifies the final equations used for numerical computation.

Finally, we require an expression for the electric field in the far-field region of S' . For this, we need to use the asymptotic expression for the radiating spherical waves

$$\lim_{\omega'r'/c \rightarrow \infty} |\omega'\lambda'm'\ell'\rangle^{(3)} \equiv (-i)^{\ell'} \mathbf{f}_{\lambda',\ell'm'}(\hat{\mathbf{r}}') \frac{e^{i\omega'(r'/c-t')}}{\omega'r'/c}, \quad (32)$$

which, from Eq. (29), readily gives the expression for the electric field in the far-field region of S' ,

$$\begin{aligned} \mathbf{E}'_s(\mathbf{r}', t') &= \sum_{\lambda'\ell'm'} \int_{0^+}^{+\infty} d\omega' \mathcal{B}'_{\lambda'\ell'm'}(\omega') (-i)^{\ell'} \\ &\times \mathbf{f}_{\lambda',\ell'm'}(\hat{\mathbf{r}}') \frac{e^{i\omega'(r'/c-t')}}{\omega'r'/c} + \text{c.c.}, \end{aligned} \quad (33)$$

where $\mathbf{f}_{\lambda',\ell'm'}(\hat{\mathbf{r}}')$ is a vector function defined in Appendix B.

As shown by Garner *et al.* [43], the angular density of the total radiation energy flux in a given direction in S' specified by θ' and ϕ' , which we denote by $U'(\theta', \phi')$, is calculated by integrating the amplitude of the electric field $\mathbf{E}'_s(\mathbf{r}', t')$ in the far-field limit. As a result, we have

$$U'(\theta', \phi') = \int_{-\infty}^{\infty} (r')^2 \frac{|\mathbf{E}'_s(\mathbf{r}', t')|^2}{\eta_0} dt', \quad (34)$$

where η_0 is the impedance of free space. An expanded and numerically efficient form of Eq. (34) is given in Appendix D.

At this point, the second step of the FHM is complete.

C. Solution to the scattering problem in the laboratory frame

To investigate the backscattering, we analyze the directivity $D(\theta, \phi)$ of the sphere. This is defined as [44]

$$D(\theta, \phi) = \frac{U(\theta, \phi)}{W_{\text{tot}}/4\pi}, \quad (35)$$

where $U(\theta, \phi) = \sum_{\lambda_s} U_{\lambda_s}(\theta, \phi)$ is the angular density of the total radiation energy in a given direction in S specified by θ and ϕ , U_{λ_s} is the component of $U(\theta, \phi)$ corresponding to the scattered helicity $\lambda_s = \pm 1$, and W_{tot} is the total scattered energy.

Considering the directivity of the sphere allows us to obtain a physically meaningful and intuitive formulation from which the behavior of the backscattering can be interpreted. Qualitatively speaking, the directivity is the ratio of the total angular energy $U(\theta, \phi)$ to the average scattered energy $W_{\text{tot}}/4\pi$ by an analogous isotropic scatterer. Consequently, a directivity greater than 1 means that the contribution of backscattered energy outweighs that of the average scattered energy. Conversely, a directivity less than 1 implies that the backscattered energy is lower than the average energy scattered by the sphere.

We are now in a position to carry out the final step of the FHM, that is, transforming the directivity from S' back to S . The power of the FHM really becomes apparent here, since the angular energy $U(\theta, \phi)$ in S can easily be related to quantities in S' . More specifically, we have

$$W_{\text{tot}} = \int_0^{2\pi} \int_0^\pi U(\theta, \phi) \sin \theta d\theta d\phi, \quad (36)$$

where, as we see from Eq. (21) in [43],

$$U(\theta, \phi) = [\gamma(1 + \beta \cos \theta')]^3 U'(\theta', \phi'), \quad (37)$$

where θ' and ϕ' can be transformed using Eqs. (14) and (16) to obtain an expression for $U(\theta, \phi)$ in S . For backscattering, we have $\theta = \Theta_{\text{BS}}$ and $\phi = \Phi_{\text{BS}}$, where

$$\Theta_{\text{BS}} = \pi - \Theta_i, \quad \Phi_{\text{BS}} = \pi, \quad (38)$$

respectively.

The third step of the FHM is now complete and the backscattered directivity D_{BS} of the sphere in S can be calculated by substituting Eqs. (36) and (37) into Eq. (35) such that

$$D_{\text{BS}} = D(\Theta_{\text{BS}}, \Phi_{\text{BS}}). \quad (39)$$

III. RELATIVISTIC KERKER CONDITION

A. Visualizing the directivity

The final theoretical result of our work has been formulated in Eq. (39), which expresses the contribution of the backscattered energy compared to the average scattered energy for a given scenario. While Eq. (35) is more general, for the sake of this discussion, we choose to investigate a possible suppression of the backscattering (that is, the first Kerker condition) [45–47].

As an example, we consider a lossless dielectric sphere and parametrize the multipolar response using what are known as Mie angles [48] (cf. Appendix E). Each Mie angle is bounded between $-\frac{\pi}{2}$ and $\frac{\pi}{2}$ and we consider them to be nondispersive. A value of zero corresponds to a resonance of the respective Mie coefficient.

Although Mie angles may seem abstract, they do carry physical meaning, and by implementing inverse design methods like that used in [49], one can design a physical spherical object that is characterized by the desired corresponding Mie coefficients, and hence desired Mie angles, which can be determined from the equations in Appendix E.

Since the objective function describing D_{BS} does not have a clear analytical solution, we implement numerical routines to identify properties for the sphere which minimize the backscattering. More specifically, we wish to seek the optimized combination of Mie angles such that the backscattering is minimized. Moreover, we first carry out the optimization when β and Θ_i are fixed values; as an example we consider $\beta = 0.2$ and $\Theta_i = \frac{\pi}{4}$.

Before doing this, it makes sense to visualize how D_{BS} varies with respect to some chosen Mie angles. For this purpose, we sweep across the possible electric quadrupole (θ_{EQ})

and magnetic quadrupole (θ_{MQ}) angles while fixing the dipole angles θ_{ED} and θ_{MD} .

We visualize the $\lambda_s = +1$ and -1 components of $\log_{10}(D_{\text{BS}})$ with $\theta_{\text{ED}} = \theta_{\text{MD}} = \pi/3$ in Figs. 4(a) and 4(b), respectively, followed by the corresponding total directivity in Fig. 4(c). In all cases, the helicity of the incident field is $\lambda_i = 1$. One observes in Fig. 4(b) for $\lambda_s = -1$ that the diagonal representing $\theta_{\text{EQ}} = \theta_{\text{MQ}}$, that is, when the sphere is a dual scatterer, displays values of below -30 , implying that the backscattering is zero at these points. This is expected, since the incoming helicity is given by $\lambda_i = +1$ and the scattered helicity in the dual case must remain the same, so we are only left with nonzero values when $\lambda_s = +1$. For comparison, Fig. 4(d) shows the total directivity for the nontrivial case where $\theta_{\text{ED}} = \pi/9$ and $\theta_{\text{MD}} = -\pi/4$.

The fact that Fig. 4(b) provides a physically known result is a justification of the numerical implementation and allows us to proceed in minimizing the directivity. A further verification is the fact that the directivity is independent of the incident helicity λ_i . This is expected since the system is both rotationally and mirror symmetric about the x axis. From the mirror symmetry, λ_i would flip sign [50]. On the other hand, when rotated to the same position, λ_i would preserve its sign. These situations, however, describe the same physical scenario, that is, a system where the sphere moves in the opposite direction with $\mathbf{v} \rightarrow -v\hat{\mathbf{z}}$ and $\Theta_i \rightarrow \pi - \Theta_i$. Therefore, the scattered energy remains unchanged.

Another way to visualize the directivity is with respect to β and Θ_i for a given set of Mie angles. This is done in Fig. 5 for $\theta_{\text{ED}} = \frac{\pi}{4}$, $\theta_{\text{EQ}} = -\frac{\pi}{9}$, $\theta_{\text{MD}} = \frac{\pi}{3}$, and $\theta_{\text{MQ}} = \frac{\pi}{7}$. First, one notices the invariance of the directivity for $\beta \rightarrow 0$. This is necessary due to the spherical symmetry of the scatterer and provides a necessary sanity check, thus increasing the credibility of the implemented code. Also noteworthy is the behavior as $\beta \rightarrow 1$. In this case, as $\Theta_i \rightarrow 0$ one sees that the directivity becomes negligibly small. This makes sense, since this scenario corresponds to the scatterer moving directly away from the source field, thus maximizing the redshift thereof (cf. Fig. 3). In accordance with Eq. (37), this corresponds to a low backscattering intensity. When $\Theta_i \rightarrow \pi$, one observes the opposite effect of strong blueshift, thus increasing the backscattering intensity.

For completion, we provide in Fig. 6 an explicit example of how D_{BS} up to octupolar order depends on the radius R of a spherical silicon carbide (SiC) particle. Here we consider the wavelength of the incident beam to be $L = 1 \mu\text{m}$ such that the relative permittivity of the particle satisfies the high-frequency limit of $\epsilon_\infty = 6.7$ [13], with a corresponding refractive index $n_{\text{SiC}} = 2.59$. Moreover, we consider an angle of incidence $\Theta_i = \frac{\pi}{4}$ and three fixed speeds, namely, $\beta = 1 \times 10^{-6}$, 0.2 , and 0.5 . One notices here that, as β increases, D_{BS} decreases. This is, once again, due to Eq. (37). Since the sphere mostly moves away from the observer in this case, the backscattering intensity viewed in S decreases. The equations for the corresponding Mie coefficients can be found in [13]. Note that, as explained in Appendix E, we consider for our purposes the negative of these expressions to conform with the passivity due to our considered time convention.

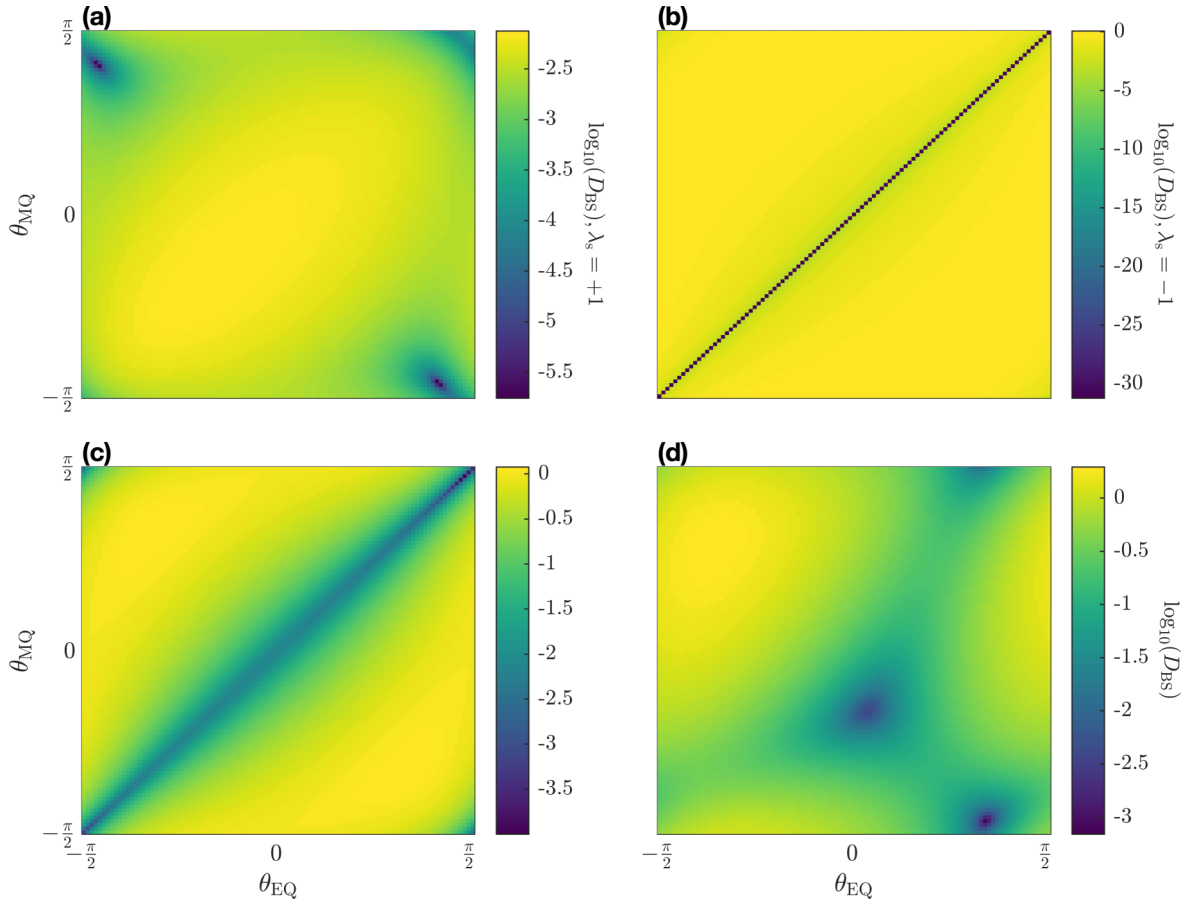


FIG. 4. The (a) $\lambda_s = +1$ and (b) $\lambda_s = -1$ components of $\log_{10}(D_{BS})$ when $\theta_{ED} = \theta_{MD} = \frac{\pi}{3}$. Note in (b) the dark diagonal line, which means that the backscattering vanishes when $\theta_{EQ} = \theta_{MQ}$. This corresponds to the case where the sphere is a dual scatterer. Since the incident helicity is given by $\lambda_i = +1$, these vanishing components are to be expected. (c) Total directivity $\log_{10}(D_{BS})$ when combining (a) and (b). (d) For comparison $\log_{10}(D_{BS})$ when $\theta_{ED} = \frac{\pi}{9}$ and $\theta_{MD} = -\frac{\pi}{4}$. In all cases, we have that $\beta = 0.2$ and $\Theta_i = \frac{\pi}{4}$.

B. Numerically minimizing the backscattering for a fixed speed and angle of incidence

To minimize the backscattering with respect to the Mie angles, we implement the directivity calculation using the

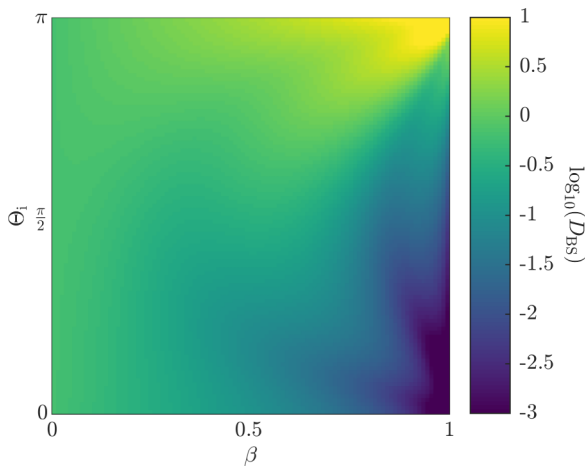


FIG. 5. Directivity D_{BS} (in \log_{10} scale) as a function of β and Θ_i with $\theta_{ED} = \frac{\pi}{4}$, $\theta_{EQ} = -\frac{\pi}{9}$, $\theta_{MD} = \frac{\pi}{3}$, and $\theta_{MQ} = \frac{\pi}{7}$.

JULIA programming language [29] and leverage the automatic differentiation capabilities included in the modeling toolkit

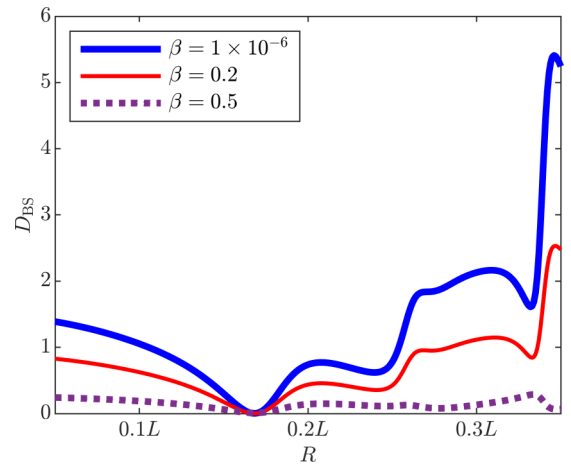


FIG. 6. Backscattered directivity D_{BS} up to octupolar order as a function of the radius R of a spherical SiC particle with refractive index $n_{SiC} = 2.59$ for a fixed angle of incidence $\Theta_i = \frac{\pi}{4}$ and three fixed speeds $\beta = 1 \times 10^{-6}$, 0.2, and 0.5. Here R is given as multiples of the wavelength $L = 1 \mu\text{m}$ of the incident beam in S.

TABLE I. Globally optimized Mie angles up to octupolar order, accompanied by the corresponding minimized directivity D_{BS} for a fixed speed $\beta = 0.2$ and angle of incidence $\Theta_i = \frac{\pi}{4}$.

θ_{ED}	θ_{MD}	θ_{EQ}	θ_{MQ}	θ_{EO}	θ_{MO}	$D_{BS} (\times 10^{-8})$
0.33	0.32	1.07	1.06	1.44	1.43	1.09

JUMP [30] for gradient-based optimization. This enables us to efficiently take derivatives of D_{BS} with respect to Mie angles up to arbitrary order.

We formulate our optimization problem as the global minimization of D_{BS} using a sequence of local optimizations [51] as implemented in the nonlinear-optimization package NLOPT [52]. We find, for a fixed speed $\beta = 0.2$ and angle of incidence $\Theta_i = \frac{\pi}{4}$, a higher-order combination of Mie angles which yield minima below our defined cutoff point of $D_C = 10^{-3}$, that is, the value below which we consider the backscattering to be negligible. We consider this value appropriate since it corresponds to a backscattered energy which contributes a mere 0.1% to the average scattered energy. For a single optimization run, we randomly initialize a set of Mie angles between $(-\frac{\pi}{2}, \frac{\pi}{2})$ and minimize D_{BS} with respect to these angles. Owing to quasianalytical gradients, the optimization quickly converges to a high-quality minimum much lower

than D_C . Finding a single set of Mie angles up to octupolar order takes less than a second on average (measured over 100 optimization runs on Intel Xeon Platinum 8368 CPU @ 2.4 GHz). The optimized Mie angles located by the global optimizer up to octupolar order and the corresponding minimized directivity D_{BS} are given in Table I.

The minimized value of $D_{BS} = 1.09 \times 10^{-8}$ is smaller than $D_C = 10^{-3}$, thus satisfying our cutoff criterion and providing evidence of the existence of the first Kerker condition in the relativistic regime. The located minimum value of D_{BS} describes a case where the backscattered energy contributes a negligible $1.09 \times 10^{-6}\%$ to the average scattered energy, thereby emphasizing its high quality. Note that there exist many combinations of Mie angles, including ones that describe a nondual system, that produce D_{BS} values below our cutoff point of $D_C = 10^{-3}$ (albeit of varying quality), making that in Table I just one of many.

C. Numerically minimizing the backscattering for varying speed and angle of incidence

An interesting extension to the results in Sec. III B is to investigate how the optimized Mie angles in Table I vary with speed β for a fixed angle of incidence Θ_i , and vice versa (cf. Fig. 7), and to find out if the globally optimized Mie angles in Table I always yield a directivity below our cutoff

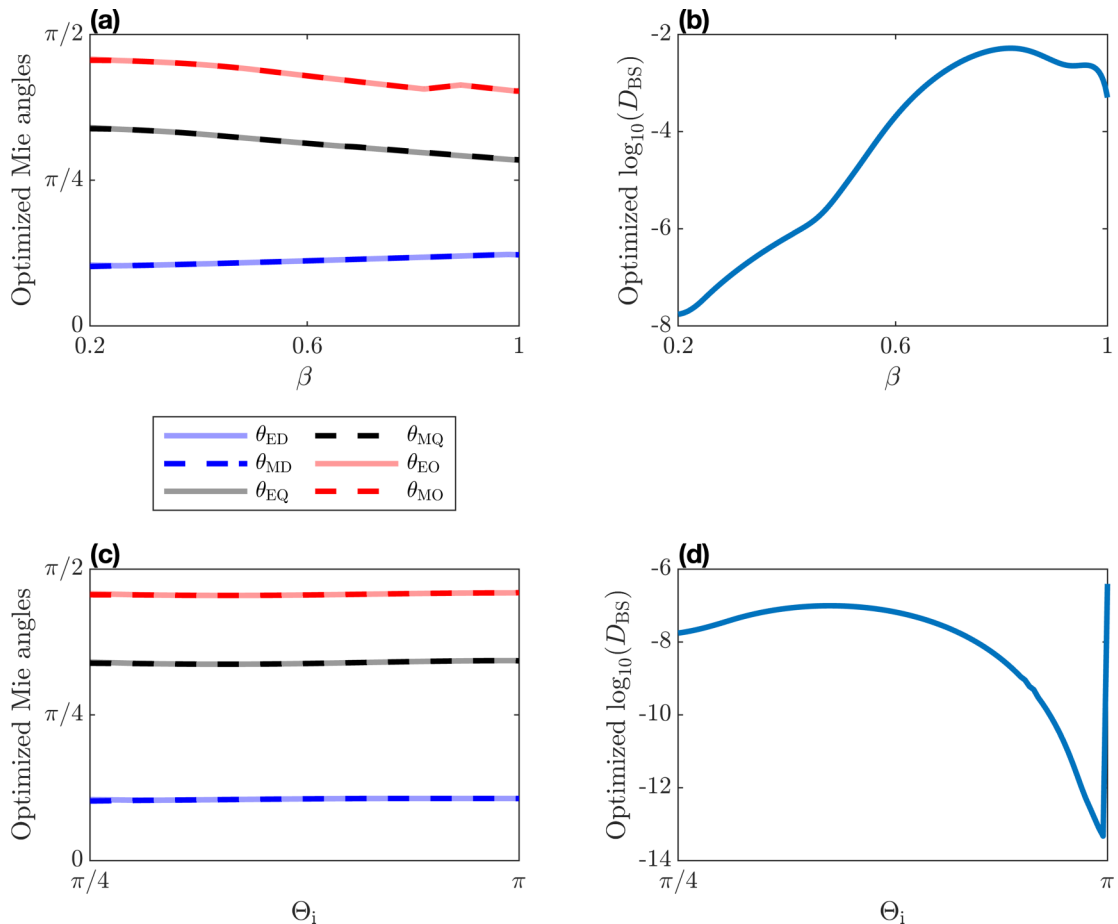


FIG. 7. Variation of the optimized (a) Mie angles and (b) directivity D_{BS} with respect to the speed β for a fixed angle of incidence $\Theta_i = \frac{\pi}{4}$. (c) and (d) analogous study but with varying Θ_i and fixed $\beta = 0.2$.

point D_C . To do this, we carry out an iterative set of local optimizations using IPOPT [53], with the Mie angles in Table I as starting points. First, β is varied slightly in each iteration for a given angle of incidence $\Theta_i = \frac{\pi}{4}$, allowing us to trace out virtually continuous curves depicting each corresponding set of optimized Mie angles, along with a curve showing the variation of the optimized directivity. For completeness, the same is done for a fixed speed $\beta = 0.2$ and varying Θ_i . Note that we do not consider lower speeds or angles of incidence, since the optimal minimized backscattering in these limits trivially occurs when the Mie angles of each order are respectively equal to each other ($\theta_{ED} = \theta_{MD}$, $\theta_{EQ} = \theta_{MQ}$, etc.). This corresponds to a dual object [54].

As seen in Figs. 7(a) and 7(c), the optimizer was able to locate Mie angles which describe a dual system for every β . In Fig. 7(b) we see that the optimized directivity has its best solution at $\beta = 0.2$, the speed at which the initial optimization was carried out. Here we have that $\log_{10}(D_{BS}) \approx -8$. The optimized directivity then increases to $\log_{10}(D_{BS}) \approx -2$ for $\beta \approx 0.8$, thus demonstrating that the globally optimized Mie angles in Table I do not always produce negligible backscattering. This means that, to locate Mie angles which produce $D_{BS} < D_C$, one would need to once again probe the parameter space of the global optimization to find a suitable combination.

As the speed increases more, the directivity decreases again, with a sharp decline occurring as $\beta \rightarrow 1$. The likely explanation for this is, as can be seen in Fig. 5, that the perceived Doppler-shifted incident frequency in S' tends to 0 as $\beta \rightarrow 1$. In line with Eq. (37), this would imply a negligible backscattered energy.

Regarding the variance with respect to the angle of incidence Θ_i , one sees in Figs. 7(c) and 7(d) that the value of $\log_{10}(D_{BS})$ always remains below the cutoff point D_C . Moreover, the optimized Mie angles essentially stay the same as the globally optimized angles in Table I, thus showing that the determined combination of optimized Mie angles vary much less with respect to Θ_i compared to β . Moreover, the minimized D_{BS} becomes more optimal for very large angles, until the limit of $\Theta_i \rightarrow \pi$ is approached, where the optimized directivity drastically increases. Analogous to before, this can again be explained by Eq. (37). An angle of incidence of $\Theta_i = \pi$ means the sphere is moving directly towards the source field. As a result, the perceived Doppler-shifted incident frequency in S' is very high, thus leading to a large backscattered energy.

Another important aspect to note is that the solutions in Fig. 7 are not unique. There exist other optimized solutions (albeit of varying quality).

IV. CONCLUSION

The main goal of this paper was to minimize the backscattered energy from a relativistically moving sphere with respect to the optical parameters thereof represented by Mie angles. In doing this, we were able to demonstrate the utility of expressing incident and scattered fields in the helicity basis using Beltrami fields. This enabled us to transform fewer variables (namely, the helicity) as opposed to the same problem in the parity basis, thus simplifying calculations. Moreover, we obtained an expression for the backscattering amplitude of the

scattered field observed from an external laboratory frame in the form of the directivity of the sphere. Finally, the backscattered energy was minimized with respect to Mie angles, the speed of the sphere, and the field angle of incidence, providing evidence for the existence of the first Kerker condition in the relativistic regime.

Opportunities for future work are plentiful. For example, the present work could be extended to analyze a composition of particles describing a metasurface as opposed to just a single particle. In this case, a cluster T matrix as described in [12] would need to be implemented. The motivation for considering a surface of particles links to the future applications of light sails proposed by the Breakthrough Starshot Initiative. Of course, this would require a refinement of the present model to consider the opposite case of maximum backscattering, resulting in the ideal case of maximum momentum transfer to the sail [55].

The code used to produce the results in this paper can be accessed via [56].

ACKNOWLEDGMENTS

M.R.W., A.G.L., and C.R. acknowledge support from the Max Planck School of Photonics, which is supported by BMBF, Max Planck Society, and the Fraunhofer Society. M.R.W. and A.G.L. also acknowledge support from the Karlsruhe School of Optics and Photonics. Y.A. and C.R. acknowledge support from the German Research Foundation within the Excellence Cluster 3D Matter Made to Order (EXC 2082/1 under Project No. 390761711) and from the Carl Zeiss Foundation. The optimizations in Sec. III were carried out on the HoreKa supercomputer funded by the Ministry of Science, Research and the Arts Baden-Württemberg and by the Federal Ministry of Education and Research.

APPENDIX A: LORENTZ BOOST OF HELICAL PLANE WAVES

As stated in [33], the Lorentz boost of the electric field $\mathbf{E}(\mathbf{r}, t)$ is given by

$$\mathbf{E}'(\mathbf{r}', t') = \gamma[\mathbf{E}(\mathbf{r}, t) + v\hat{\mathbf{v}} \times \mathbf{B}(\mathbf{r}, t)] + (1-\gamma)[\hat{\mathbf{v}} \cdot \mathbf{E}(\mathbf{r}, t)]\hat{\mathbf{v}}, \quad (\text{A1})$$

where $\mathbf{B}(\mathbf{r}, t)$ is the corresponding magnetic field and $\gamma = 1/\sqrt{1-\beta^2}$, with $\beta = v/c$ the ratio of the boosting speed to the speed of light, and boosting takes place in the $\hat{\mathbf{v}}$ direction. For boosting along $+\hat{\mathbf{z}}$, the coordinates of the primed (boosted) and unprimed coordinate systems are related to the following formulas:

$$x' = x, \quad (\text{A2})$$

$$y' = y, \quad (\text{A3})$$

$$z' = \gamma(z - \beta ct), \quad (\text{A4})$$

$$t' = \gamma(t - \beta z/c). \quad (\text{A5})$$

Here we want to consider the boost of a monochromatic plane wave of well-defined helicity λ . Specifically, its electric field

is given by $\mathbf{E}(\mathbf{r}, t) = \hat{\mathbf{e}}_\lambda(\hat{\mathbf{k}}) \exp\{i\omega[(\hat{\mathbf{k}} \cdot \mathbf{r}/c) - t]\}$ (discussed in the main text). By making use of the above coordinate transformations, we can get the following transformation of the exponent: $\{i\omega[(\hat{\mathbf{k}} \cdot \mathbf{r}/c) - t]\} = \{i\omega'[(\hat{\mathbf{k}}' \cdot \mathbf{r}'/c) - t']\}$, with ω' and $\hat{\mathbf{k}}'$ given by Eqs. (15) and (17), respectively. Thus, we have transformed the scalar part of the fields, which gave us the transformed frequency and direction of propagation of the boosted plane wave, ω' and $\hat{\mathbf{k}}'$, respectively.

Next we need to transform the polarization vector. For this, we need to take into account that our considered plane wave, being an eigenstate of the helicity operator $\frac{\nabla \times}{k}$ with well-defined helicity λ [41,57], has the property

$$\nabla \times \mathbf{E}(\mathbf{r}, t) = \lambda k \mathbf{E}(\mathbf{r}, t), \quad (\text{A6})$$

and therefore we get the following for its corresponding magnetic field from Maxwell's equations:

$$\mathbf{B}(\mathbf{r}, t) = \frac{\lambda}{ic} \mathbf{E}(\mathbf{r}, t). \quad (\text{A7})$$

Therefore, by substituting the right-hand side of Eq. (A7) into Eq. (A1), we find that

$$\begin{aligned} \mathbf{E}'(\mathbf{r}', t') &= \gamma \left(\mathbf{E}(\mathbf{r}, t) + \frac{\lambda v}{ic} \hat{\mathbf{z}} \times \mathbf{E}(\mathbf{r}, t) \right) \\ &+ (1 - \gamma) [\hat{\mathbf{z}} \cdot \mathbf{E}(\mathbf{r}, t)] \hat{\mathbf{z}}. \end{aligned} \quad (\text{A8})$$

What remains then is to project the boosted helical polarization vector $\hat{\mathbf{e}}_\lambda(\hat{\mathbf{k}})$ onto the boosted polarization basis $\hat{\mathbf{e}}_{\lambda'}(\hat{\mathbf{k}}')$. Specifically, we need to find the coefficients $\mathcal{E}_{\lambda\lambda'}(\beta, \hat{\mathbf{k}})$ in the expansion below:

$$\begin{aligned} \gamma \left(\hat{\mathbf{e}}_\lambda(\hat{\mathbf{k}}) + \frac{\lambda v}{ic} \hat{\mathbf{z}} \times \hat{\mathbf{e}}_\lambda(\hat{\mathbf{k}}) \right) &+ (1 - \gamma) [\hat{\mathbf{z}} \cdot \hat{\mathbf{e}}_\lambda(\hat{\mathbf{k}})] \hat{\mathbf{z}} \\ &= \sum_{\lambda'} \mathcal{E}_{\lambda\lambda'}(\beta, \hat{\mathbf{k}}) \hat{\mathbf{e}}_{\lambda'}(\hat{\mathbf{k}}'). \end{aligned} \quad (\text{A9})$$

By making use of the orthogonality relation [50]

$$\hat{\mathbf{e}}_{\lambda'}(\hat{\mathbf{k}}') \cdot \hat{\mathbf{e}}_{-\lambda'_0}(\hat{\mathbf{k}}') = -\delta_{\lambda'\lambda'_0}, \quad (\text{A10})$$

we readily get after some algebra that $\mathcal{E}_{\lambda\lambda'}(\beta, \hat{\mathbf{k}}) = \delta_{\lambda\lambda'} C_\lambda(\beta, \theta)$, with θ the polar angle of the propagation direction $\hat{\mathbf{k}}$ and $C_\lambda(\beta, \theta)$ given by

$$C_\lambda(\beta, \theta) = \gamma(1 - \beta \cos \theta). \quad (\text{A11})$$

The same expression calculated using the parity basis is given by Eq. (27) in [38]. Note that the helicity λ of massless particles (and hence electromagnetic fields) is invariant under Lorentz boosts [40]. Finally, summing up all the above, we get the Lorentz boost transformation given by Eq. (11).

APPENDIX B: VECTOR SPHERICAL HARMONICS OF WELL-DEFINED HELICITY

We begin by using the definition of the spherical harmonics

$$Y_\ell^m(\theta, \phi) \triangleq \Omega_{\ell m} P_\ell^m(\cos \theta) e^{im\phi}, \quad (\text{B1})$$

where $P_\ell^m(\cos \theta)$ is the associated Legendre function of the first kind, with $\Omega_{\ell m} \triangleq i^m \sqrt{\frac{(2\ell+1)(\ell-m)!}{4\pi\ell(\ell+1)(\ell+m)!}}$ the corresponding

normalization factor. Then the VSHs of well-defined parity, $\mathbf{M}_{\ell m k}^{(j)}$ and $\mathbf{N}_{\ell m k}^{(j)}$, are defined as [58]

$$\begin{aligned} \mathbf{M}_{\ell m k}^{(j)}(\mathbf{r}) &\triangleq \nabla \times [\mathbf{r} z_{M,\ell}^{(j)}(kr) Y_\ell^m(\theta, \phi)] \\ &= i z_{M,\ell}^{(j)}(kr) \mathbf{m}_{\ell m}(\hat{\mathbf{r}}), \end{aligned} \quad (\text{B2})$$

$$\begin{aligned} \mathbf{N}_{\ell m k}^{(j)}(\mathbf{r}) &\triangleq \frac{1}{k} \nabla \times \mathbf{M}_{\ell m k}^{(j)}(\mathbf{r}) \\ &= \hat{\mathbf{r}} \frac{\ell(\ell+1)}{k_0 r} z_{M,\ell}^{(j)}(kr) Y_\ell^m(\theta, \phi) + z_{N,\ell}^{(j)}(kr) \mathbf{n}_{\ell m}(\hat{\mathbf{r}}), \end{aligned} \quad (\text{B3})$$

where

$$\mathbf{m}_{\ell m}(\hat{\mathbf{r}}) = \Omega_{\ell m} [\hat{\theta} \tau_{\ell m}(\theta) + i \hat{\phi} \tau'_{\ell m}(\theta)] e^{im\phi}, \quad (\text{B4})$$

$$\mathbf{n}_{\ell m}(\hat{\mathbf{r}}) = \Omega_{\ell m} [\hat{\theta} \tau'_{\ell m}(\theta) + i \hat{\phi} \tau_{\ell m}(\theta)] e^{im\phi}. \quad (\text{B5})$$

The index ℓ stands for the angular momentum quantum number that takes the values $1, 2, \dots$ and corresponds to dipoles, quadrupoles, etc., and the index m stands for the angular momentum along the z axis which takes the values $-\ell, \dots, -2, -1, 0, 1, 2, \dots, \ell$. The superscript j refers to the corresponding Bessel ($j=1$) and Hankel ($j=3$) functions, $z_{M,\ell}^{(j)}(kr)$, of the first kind. The functions $z_{N,\ell}^{(j)}(kr) \triangleq \frac{1}{kr} \frac{d}{d(kr)} [kr z_{M,\ell}^{(j)}(kr)]$ are the corresponding Riccati functions and $\tau_{\ell m}(\theta) \triangleq m \frac{P_\ell^m(\cos \theta)}{\sin \theta}$ and $\tau'_{\ell m}(\theta) \triangleq \frac{dP_\ell^m(\cos \theta)}{d\theta}$ are the generalized Legendre functions.

The VSHs $\Lambda_{\lambda,\ell m k}^{(j)}(\mathbf{r})$ of well-defined helicity $\lambda = \pm 1$ are defined with respect to the VSHs of well-defined parity according to the formula [41]

$$\begin{aligned} \Lambda_{\lambda,\ell m k}^{(j)}(\mathbf{r}) &= \frac{\mathbf{M}_{\ell m k}^{(j)}(\mathbf{r}) + \lambda \mathbf{N}_{\ell m k}^{(j)}(\mathbf{r})}{\sqrt{2}} \\ &= \frac{\lambda}{\sqrt{2}} \frac{\ell(\ell+1)}{kr} z_{M,\ell}^{(j)}(kr) Y_\ell^m(\theta, \phi) \hat{\mathbf{r}} \\ &+ \sum_{\lambda'=\pm 1} \left(\frac{i z_{M,\ell}^{(j)}(kr) + \lambda \lambda' z_{N,\ell}^{(j)}(kr)}{2} \cdot \mathbf{f}_{\lambda',\ell m}(\hat{\mathbf{r}}) \right), \end{aligned} \quad (\text{B6})$$

where we have defined

$$\begin{aligned} \mathbf{f}_{\lambda,\ell m}(\hat{\mathbf{r}}) &= \frac{\mathbf{m}_{\ell m}(\hat{\mathbf{r}}) + \lambda \mathbf{n}_{\ell m}(\hat{\mathbf{r}})}{\sqrt{2}} \\ &= \Omega_{\ell m} \tau_{\ell m}^{(\lambda)}(\theta) e^{im\phi} \hat{\mathbf{e}}_\lambda(\hat{\mathbf{r}}) \end{aligned} \quad (\text{B8})$$

and

$$\tau_{\ell m}^{(\lambda)}(\theta) = -\tau'_{\ell m}(\theta) - \lambda \tau_{\ell m}(\theta), \quad (\text{B9})$$

which has the property $\Omega_{-\ell m} \tau_{-\ell m}^{(\lambda)}(\theta) = \Omega_{\ell m} \tau_{\ell m}^{(-\lambda)}(\theta) = (-1)^{\ell+m+1} \Omega_{\ell m} \tau_{\ell m}^{(\lambda)}(\pi - \theta)$. One can show that the functions $\Lambda_{\lambda,\ell m k}^{(j)}$ have the property [41]

$$\frac{\nabla \times}{k} \Lambda_{\lambda,\ell m k}^{(j)} = \lambda \Lambda_{\lambda,\ell m k}^{(j)}, \quad (\text{B10})$$

that is, $\Lambda_{\lambda,\ell m k}^{(j)}$ is an eigenstate of the helicity operator $\frac{\nabla \times}{k}$ with eigenvalue λ . For the functions $\mathbf{f}_{\lambda,\ell m}$, there exists the

orthogonality property

$$\int_0^{2\pi} d\phi \int_0^\pi \sin\theta d\theta \mathbf{f}_{\lambda, \ell m}(\hat{\mathbf{k}}) \cdot [\mathbf{f}_{\lambda', \ell' m'}(\hat{\mathbf{k}})]^* = \delta_{\lambda\lambda'} \delta_{\ell\ell'} \delta_{m'm'}. \quad (\text{B11})$$

Moreover, if we employ the large argument property of the Hankel functions

$$z_{\alpha, \ell}^{(3)}(x) \xrightarrow{x \gg 1} \begin{cases} \frac{e^{ix}}{x} (-i)^\ell & \text{for } \alpha = \text{N} \\ \frac{e^{ix}}{x} (-i)^{\ell+1} & \text{for } \alpha = \text{M}, \end{cases} \quad (\text{B12})$$

and also reject the $O(1/r_0^2)$ radial term as negligible, for the radiating helical VSHs we can get the following asymptotic form in the far field:

$$[\mathbf{A}_{\lambda, \ell m k}^{(3)}(\mathbf{r})]^{\text{ff}} = (-i)^\ell \mathbf{f}_{\lambda, \ell m}(\hat{\mathbf{r}}) \frac{e^{ikr}}{kr}. \quad (\text{B13})$$

APPENDIX C: THE T MATRIX IN THE HELICITY BASIS FOR A SPHERE

In the parity basis, the T matrix is given by

$$\mathbf{T} = \begin{pmatrix} \mathbf{T}_{\text{NN}} & \mathbf{T}_{\text{MN}} \\ \mathbf{T}_{\text{NM}} & \mathbf{T}_{\text{MM}} \end{pmatrix}, \quad (\text{C1})$$

where each element of Eq. (C1) is a diagonal $\ell_{\text{max}}(2 + \ell_{\text{max}}) \times \ell_{\text{max}}(2 + \ell_{\text{max}})$ matrix and ℓ_{max} is the maximum multipolar excitation order of the sphere. This can be transformed to the T matrix \mathbf{T}^{H} in the helicity basis by using [59]

$$\mathbf{T}^{\text{H}} = \mathbf{P}^{-1} \mathbf{T} \mathbf{P}, \quad (\text{C2})$$

where, as can be seen from Eq. (2), \mathbf{P} is given by

$$\mathbf{P} = \frac{1}{\sqrt{2}} \begin{pmatrix} 1 & 1 \\ 1 & -1 \end{pmatrix}. \quad (\text{C3})$$

In the case of a dielectric sphere, we have that $\mathbf{T}_{\text{MN}} = \mathbf{T}_{\text{NM}} = 0$, so Eq. (C2) reduces to

$$\begin{aligned} \mathbf{T}^{\text{H}} &= \begin{pmatrix} \mathbf{T}_{++} & \mathbf{T}_{+-} \\ \mathbf{T}_{-+} & \mathbf{T}_{--} \end{pmatrix} \\ &= \frac{1}{2} \begin{bmatrix} \mathbf{T}_{\text{NN}} + \mathbf{T}_{\text{MM}} & \mathbf{T}_{\text{NN}} - \mathbf{T}_{\text{MM}} \\ \mathbf{T}_{\text{NN}} - \mathbf{T}_{\text{MM}} & \mathbf{T}_{\text{NN}} + \mathbf{T}_{\text{MM}} \end{bmatrix}, \end{aligned} \quad (\text{C4})$$

where

$$\mathbf{T}_{\text{NN}} = \begin{pmatrix} a_1 & \cdots & 0 \\ \vdots & \ddots & \vdots \\ 0 & \cdots & a_{\ell_{\text{max}}} \end{pmatrix}, \quad (\text{C5})$$

$$\mathbf{T}_{\text{MM}} = \begin{pmatrix} b_1 & \cdots & 0 \\ \vdots & \ddots & \vdots \\ 0 & \cdots & b_{\ell_{\text{max}}} \end{pmatrix}, \quad (\text{C6})$$

and the values a_ℓ and b_ℓ are the electric and magnetic Mie coefficients, respectively, defined in Appendix E. The components of the T matrix \mathbf{T}^{H} are given by $T_{\lambda_s, \lambda_i, \ell}$ and relate to the entries in \mathbf{T}^{H} corresponding to the ℓ th multipolar order, along with an incident helicity λ_i and scattered helicity λ_s , that is,

$$T_{\lambda_s, \lambda_i, \ell} = a_\ell + \lambda_i \lambda_s b_\ell. \quad (\text{C7})$$

APPENDIX D: COMPUTATION-FRIENDLY EXPANSION OF EQ. (34)

By substituting Eq. (33) into Eq. (34) and using the orthogonality relation given by Eq. (B11), we can express the angular energy density $U'(\theta', \phi')$ in the form that is suitable for efficient numerical evaluation,

$$\begin{aligned} U'(\theta', \phi') &= \sum_{\lambda'} \frac{4\pi c^2}{\eta_0} \int_{0^+}^\infty d\omega' \\ &\times \frac{1}{(\omega')^2} \left| \sum_{\ell' m'} \mathcal{B}_{\lambda' \ell' m'}(\omega') (-i)^{\ell'} \Omega_{\ell' m'} \tau_{\ell' m'}^{(\lambda')}(\theta') e^{i\ell' \phi'} \right|^2 \\ &= \sum_{\lambda'} \sum_{\ell' m'} \sum_{\bar{\ell}' \bar{m}'} \mathcal{Q}_{\lambda' \ell' m'}^{\bar{\ell}' \bar{m}'}(\theta', \phi') \sum_{\lambda_0 \bar{\lambda}_0} J_{\lambda_0 \ell' m'}^{\bar{\lambda}_0 \bar{\ell}' \bar{m}'} T_{\lambda' \lambda_0, \ell'} T_{\lambda' \bar{\lambda}_0, \bar{\ell}'}^*, \end{aligned} \quad (\text{D1})$$

where the T -matrix elements $T_{\lambda' \lambda_0, \ell'}$ are defined in Appendix C. For the second equality, we have assumed a nondispersive T matrix and have also defined the integral

$$J_{\lambda_0 \ell' m'}^{\bar{\lambda}_0 \bar{\ell}' \bar{m}'} = \int_{0^+}^\infty d\omega' \frac{\mathcal{A}_{\lambda_0 \ell' m'}(\omega') \mathcal{A}_{\bar{\lambda}_0 \bar{\ell}' \bar{m}'}^*(\omega')}{(\omega')^2} \quad (\text{D2})$$

and the quantity

$$\begin{aligned} \mathcal{Q}_{\lambda' \ell' m'}^{\bar{\ell}' \bar{m}'}(\theta', \phi') &= \frac{4\pi c^2}{\eta_0} (-i)^{\ell' - \bar{\ell}'} \Omega_{\ell' m'} \Omega_{\bar{\ell}' \bar{m}'}^* \tau_{\ell' m'}^{(\lambda')}(\theta') \tau_{\bar{\ell}' \bar{m}'}^{(\lambda')*}(\theta') \\ &\times e^{i(m' - \bar{m}') \phi'}, \end{aligned} \quad (\text{D3})$$

where the asterisk denotes the complex conjugate. Furthermore, we can express the total scattered energy W_{tot} given by Eq. (36) as

$$\begin{aligned} W_{\text{tot}} &= \int_0^\pi d\theta \int_0^{2\pi} d\phi \sin\theta U(\theta, \phi) \\ &= \sum_{\lambda'} \int_{0^+}^\infty d\omega' \frac{1}{(\omega')^2} \\ &\times \sum_{\ell' m'; \min\{|m'|, 1\} \leq \ell' \leq \ell'} \text{Re}(\mathcal{B}_{\omega' \lambda' \ell' m'} \mathcal{B}_{\omega' \lambda' \ell' m'}^* I_{\lambda' \ell' m'}^\ell) \\ &= \sum_{\lambda'} \sum_{\ell' m'; \min\{|m'|, 1\} \leq \ell' \leq \ell} \sum_{\lambda_0 \bar{\lambda}_0} \text{Re}(I_{\lambda' \ell' m'}^\ell J_{\lambda_0 \ell' m'}^{\bar{\lambda}_0 \bar{\ell}' \bar{m}'} T_{\lambda' \lambda_0, \ell'} T_{\lambda' \bar{\lambda}_0, \bar{\ell}'}^*), \end{aligned} \quad (\text{D4})$$

with

$$\begin{aligned} I_{\lambda' \ell' m'}^\ell &= 2^{4 - \delta_{\ell \ell'}} \frac{\pi^2 c^2}{\eta_0} (-i)^{\ell' - \ell} \Omega_{\ell' m'} \Omega_{\ell m'}^* \\ &\times \int_0^\pi d\theta \sin\theta \{\gamma [1 + \beta \cos[\theta'(\beta, \theta)]]\}^3 \\ &\times \tau_{\ell' m'}^{(\lambda')}[\theta'(\beta, \theta)] \tau_{\ell m'}^{(\lambda')*}[\theta'(\beta, \theta)], \end{aligned} \quad (\text{D5})$$

where the expression for $\theta'(\beta, \theta)$ is given by Eq. (14).

Note the importance of writing Eq. (D1) as nested integrals instead of a standard triple integral. Computationally speaking, we are able to determine Eq. (D2) with a very low tolerance, while using a higher tolerance for the other integrals, thus significantly reducing computation time. The reason for this is because the expansion coefficients $\mathcal{A}_{\lambda' \ell' m'}(\omega')$

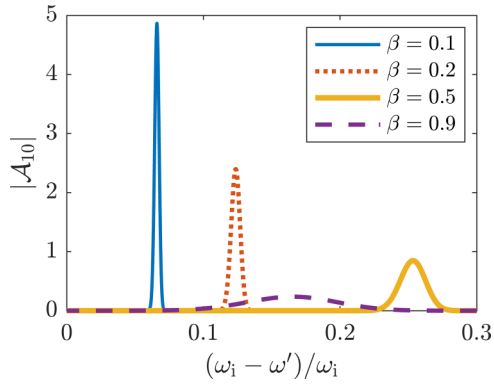


FIG. 8. Absolute value of the dipole expansion coefficients \mathcal{A}_{10} ($\ell' = 1, m' = 0$) given by Eq. (27) as a function of the normalized frequency $(\omega_i - \omega')/\omega_i$ when $\beta = 0.1$ (blue solid line), $\beta = 0.2$ (orange dotted line), $\beta = 0.5$ (yellow thick solid line), and $\beta = 0.9$ (purple dashed line). In all cases, $\Theta_i = \frac{\pi}{4}$ and $\lambda_i = +1$ which, since helicity is conserved under Lorentz boosts, means that $\lambda' = \lambda_i = +1$. Note that the width of the peak increases with speed. This is due to the increasing effect of the Doppler shift ω' of ω_i . Since the incident beam is monochromatic, $|\mathcal{A}_{10}|$ tends to a δ -distribution-like peak as the speed decreases. As the speed increases, the plane-wave components of the incident beam all Doppler shift differently due to their differing angular orientations. This leads to nonzero values for $|\mathcal{A}_{10}|$ when $\omega_i \neq \omega'$.

[and hence the integrand in Eq. (D2)] form Gaussian-like peaks centered about ω' which tend to a δ distribution as the speed of the sphere decreases (see Fig. 8). If the tolerance is too high, the numerical integration could miss this peak entirely, thus ignoring vital nonzero values.

Moreover, by separating the integrals (D4) we are able to obtain 100×100 grids for the directivity (like those used to generate Fig. 4) in as little as approximately 40 s. The reason for this is that, as the numerically demanding integral $J_{\lambda_0 \ell' m'}$ is independent of the Mie angles, we only need to compute it once for a given angle of incidence Θ_i and speed parameter β . If the integrals were combined, $J_{\lambda_0 \ell' m'}$ would be computed for each combination of Mie angles, thus significantly increasing computation time.

APPENDIX E: MIE ANGLES FOR A LOSSLESS SPHERE

The electric and magnetic Mie coefficients a_ℓ and b_ℓ for each multipolar order ℓ can be represented using Mie angles $\theta_{E\ell}$ and $\theta_{M\ell}$, respectively. In the lossless case, one can write [28,48]

$$a_\ell = -i \sin \alpha_\ell \exp(-i\alpha_\ell) \quad (\text{E1})$$

and

$$b_\ell = -i \sin \beta_\ell \exp(-i\beta_\ell), \quad (\text{E2})$$

where

$$\alpha_\ell = \frac{\pi}{2} - \theta_{E\ell}, \quad -\frac{\pi}{2} \leq \theta_{E\ell} \leq \frac{\pi}{2}, \quad (\text{E3})$$

and

$$\beta_\ell = \frac{\pi}{2} - \theta_{M\ell}, \quad -\frac{\pi}{2} \leq \theta_{M\ell} \leq \frac{\pi}{2}. \quad (\text{E4})$$

Note that the convention used in [28] omits the use of the minus sign in Eqs. (E1) and (E2). In our case, the minus sign is required to conform with the passivity due to our considered time convention.

-
- [1] D. Sinclair, *J. Opt. Soc. Am.* **37**, 475 (1947).
[2] D. Kunz, A. Thurn, and W. Burchard, *Colloid Polym. Sci.* **261**, 635 (1983).
[3] R. Graaff, J. Aarnoudse, J. R. Zijp, P. Sloot, F. De Mul, J. Greve, and M. Koelink, *Appl. Opt.* **31**, 1370 (1992).
[4] D. Tzarouchis and A. Sihvola, *Appl. Sci.* **8**, 184 (2018).
[5] W. Mundy, J. Roux, and A. Smith, *J. Opt. Soc. Am.* **64**, 1593 (1974).
[6] C. Sorensen and D. Fischbach, *Opt. Commun.* **173**, 145 (2000).
[7] T. Wriedt, in *The Mie Theory: Basics and Applications*, edited by W. Hergert and T. Wriedt, Springer Series in Optical Sciences Vol. 169 (Springer, Berlin, 2012), pp. 53–71.
[8] R. Drake and J. Gordon, *Am. J. Phys.* **53**, 955 (1985).
[9] Y.-L. Geng, X.-B. Wu, L.-W. Li, and B.-R. Guan, *Phys. Rev. E* **70**, 056609 (2004).
[10] Y. Pavlyukh and W. Hübner, *Phys. Rev. B* **70**, 245434 (2004).
[11] R. Hightower and C. Richardson, *Appl. Opt.* **27**, 4850 (1988).
[12] M. I. Mishchenko, L. D. Travis, and A. A. Lacis, *Scattering, Absorption, and Emission of Light by Small Particles* (Cambridge University Press, Cambridge, 2002).
[13] C. F. Bohren and D. R. Huffman, *Absorption and Scattering of Light by Small Particles* (Wiley, New York, 2008).
[14] H. K. Shamkhi, K. V. Baryshnikova, A. Sayanskiy, P. Kapitanova, P. D. Terekhov, P. Belov, A. Karabchevsky, A. B. Evlyukhin, Y. Kivshar, and A. S. Shalin, *Phys. Rev. Lett.* **122**, 193905 (2019).
[15] W. Liu and Y. S. Kivshar, *Opt. Express* **26**, 13085 (2018).
[16] A. V. Poshakinskiy and A. N. Poddubny, *Phys. Rev. X* **9**, 011008 (2019).
[17] V. E. Babicheva and A. B. Evlyukhin, *Laser Photon. Rev.* **11**, 1700132 (2017).
[18] H. K. Shamkhi, A. Sayanskiy, A. C. Valero, A. S. Kupriianov, P. Kapitanova, Y. S. Kivshar, A. S. Shalin, and V. R. Tuz, *Phys. Rev. Mater.* **3**, 085201 (2019).
[19] J. Olmos-Trigo, C. Sanz-Fernández, D. R. Abujetas, J. Las-Alonso, N. de Sousa, A. Garcia-Etxarri, J. A. Sánchez-Gil, G. Molina-Terriza, and J. J. Sáenz, *Phys. Rev. Lett.* **125**, 073205 (2020).
[20] R. Alae, R. Filter, D. Lehr, F. Lederer, and C. Rockstuhl, *Opt. Lett.* **40**, 2645 (2015).
[21] X. Zhang, J. Li, J. F. Donegan, and A. L. Bradley, *Phys. Rev. Mater.* **4**, 125202 (2020).
[22] H. Barhom, A. A. Machnev, R. E. Noskov, A. Goncharenko, E. A. Gurvitz, A. S. Timin, V. A. Shkoldin, S. V. Koniakhin, O. Y. Koval, M. V. Zyuzin *et al.*, *Nano Lett.* **19**, 7062 (2019).
[23] V. Asadchy, A. G. Lampranidis, G. Ptitcyn, M. Albooyeh, T. Karamanos, R. Alae, S. A. Tretyakov, C. Rockstuhl, and S. Fan, *Phys. Rev. Appl.* **18**, 054065 (2022).

- [24] M. M. Bukharin, V. Y. Pecherkin, A. K. Ospanova, V. B. Il'in, L. M. Vasilyak, A. A. Basharin, and B. Luk'yanchuk, *Sci. Rep.* **12**, 7997 (2022).
- [25] X. Zambrana-Puyalto, I. Fernandez-Corbaton, M. Juan, X. Vidal, and G. Molina-Terriza, *Opt. Lett.* **38**, 1857 (2013).
- [26] K. L. Parkin, *Acta Astronaut.* **152**, 370 (2018).
- [27] P. Daukantas, S. Michaud, I. Ostrin, and S. Wills, *Opt. Photon. News* **28**, 8 (2017).
- [28] A. Rahimzadegan, R. Alaei, C. Rockstuhl, and R. W. Boyd, *Opt. Express* **28**, 16511 (2020).
- [29] J. Bezanson, A. Edelman, S. Karpinski, and V. B. Shah, *SIAM Rev.* **59**, 65 (2017).
- [30] I. Dunning, J. Huchette, and M. Lubin, *SIAM Rev.* **59**, 295 (2017).
- [31] T. W. Hughes, I. A. Williamson, M. Minkov, and S. Fan, *ACS Photon.* **6**, 3010 (2019).
- [32] M. Minkov, I. A. Williamson, L. C. Andreani, D. Gerace, B. Lou, A. Y. Song, T. W. Hughes, and S. Fan, *ACS Photon.* **7**, 1729 (2020).
- [33] T. J. Garner, A. Lakhtakia, J. K. Breakall, and C. F. Bohren, *J. Opt. Soc. Am. A* **34**, 270 (2017).
- [34] A. Lakhtakia, *Beltrami Fields in Chiral Media* (World Scientific, Singapore, 1994), Vol. 2.
- [35] A. Lakhtakia, *Optik (Stuttgart)* **88**, 187 (1991).
- [36] J. Etnyre and R. Ghrist, *Nonlinearity* **13**, 441 (2000).
- [37] A. Enciso and D. Peralta-Salas, *Arch. Ration. Mech. Anal.* **220**, 243 (2016).
- [38] P. De Cupis, G. Gerosa, and G. Schettini, *J. Electromagn. Waves Appl.* **14**, 1037 (2000).
- [39] A. G. Lamprianidis and A. E. Miroschnichenko, *Beilstein J. Nanotech.* **9**, 1478 (2018).
- [40] I. Fernandez-Corbaton, *Frontiers in Optics 2015* (Optica Publishing Group, 2015), paper No. LM1H.2.
- [41] C. F. Bohren, *Chem. Phys. Lett.* **29**, 458 (1974).
- [42] A. Lakhtakia, *Optik (Stuttgart)* **91**, 35 (1992).
- [43] T. J. Garner, A. Lakhtakia, J. K. Breakall, and C. F. Bohren, *Phys. Rev. A* **96**, 053839 (2017).
- [44] D. Poljak and M. Cvetkovic, *Human Interaction with Electromagnetic Fields: Computational Models in Dosimetry* (Academic, New York, 2019).
- [45] M. Dubois, L. Leroi, Z. Raolison, R. Abdeddaim, T. Antonakakis, J. de Rosny, A. Vignaud, P. Sabouroux, E. Georget, B. Larrat, G. Tayeb, N. Bonod, A. Amadon, F. Mauconduit, C. Poupon, D. Le Bihan, and S. Enoch, *Phys. Rev. X* **8**, 031083 (2018).
- [46] Z. Zhang, Z. Che, X. Liang, J. Chu, J. Zeng, H. Huang, F. Guan, L. Shi, X. Liu, and J. Zi, *Phys. Rev. Appl.* **16**, 054017 (2021).
- [47] L. Xiong, X. Zhao, X. Du, S. Chen, Y. Lu, H. Ding, and G. Li, *Nano Res.* **16**, 3195 (2023).
- [48] H. C. van de Hulst, *Light Scattering by Small Particles* (Dover, Mineola, 1981).
- [49] L. Kuhn, T. Repän, and C. Rockstuhl, *Sci. Rep.* **12**, 19019 (2022).
- [50] A. G. Lamprianidis, X. Zambrana-Puyalto, C. Rockstuhl, and I. Fernandez-Corbaton, *Laser Photon. Rev.* **16**, 2000516 (2022).
- [51] A. H. G. Rinnooy Kan and G. T. Timmer, *Math. Program.* **39**, 27 (1987).
- [52] S. G. Johnson, The NLOpt nonlinear-optimization package, <https://github.com/stevengj/nlopt> (2007).
- [53] A. Wächter, in *Machine Learning Approaches to Statistical Dependences and Causality*, edited by D. Janzing, S. Lauritzen, and B. Schölkopf, *Dagstuhl Seminar Proceedings Vol. 9401* (Schloss Dagstuhl, Dagstuhl, 2009).
- [54] M. Kerker, D.-S. Wang, and C. Giles, *J. Opt. Soc. Am.* **73**, 765 (1983).
- [55] H.-T. Tung and A. R. Davoyan, *Nano Lett.* **22**, 1108 (2022).
- [56] <https://github.com/tfp-photonics/Jorkle.jl>.
- [57] I. Fernandez-Corbaton, *Phys. Rev. B* **103**, 054406 (2021).
- [58] H. Feshbach and P. M. Morse, *Methods of Theoretical Physics* (McGraw-Hill, New York, 1953).
- [59] A. Rahimzadegan, C. Rockstuhl, and I. Fernandez-Corbaton, *Phys. Rev. Appl.* **9**, 054051 (2018).